

1      **High-level cognition is supported by at least second order**  
2      **dynamic correlations in neural activity patterns**

3      Lucy L. W. Owen<sup>1</sup>, Thomas H. Chang<sup>1,2</sup>, and Jeremy R. Manning<sup>1,†</sup>

<sup>1</sup>Department of Psychological and Brain Sciences,  
Dartmouth College, Hanover, NH

<sup>3</sup>Amazon.com, Seattle, WA

<sup>†</sup>Address correspondence to jeremy.r.manning@dartmouth.edu

4      September 4, 2019

5      **Abstract**

6      Our thoughts arise from coordinated patterns of interactions between brain structures that change  
7      with our ongoing experiences. High-order dynamic correlations in brain activity patterns reflect different  
8      subgraphs of the brain’s connectome that display homologous lower-level dynamic correlations. We tested  
9      the hypothesis that high-level cognition is supported by high-order dynamic correlations in brain activity  
10     patterns. We developed an approach to estimating high-order dynamic correlations in timeseries data,  
11     and we applied the approach to neuroimaging data collected as human participants either listened to a  
12     ten-minute story or a temporally scrambled version of the story, or underwent a resting state scan. We  
13     trained across-participants pattern classifiers to decode (in held-out data) when in the session each activity  
14     snapshot was collected. We found that classifiers trained to decode from high-order dynamic correlations  
15     yielded better performance on data collected as participants listened to the (unscrambled) story. By  
16     contrast, classifiers trained to decode data from scrambled versions of the story or during the resting  
17     state scan yielded the best performance when they were trained using first-order dynamic correlations  
18     or raw activity patterns. We suggest that as our thoughts become more complex, they are supported by  
19     higher-order patterns of dynamic network interactions throughout the brain.

20     **Introduction**

21     A central goal in cognitive neuroscience is to elucidate the *neural code*: the mapping between (a) mental  
22     states or cognitive representations and (b) neural activity patterns. One means of testing models of the  
23     neural code is to ask how accurately that model is able to “translate” neural activity patterns into known  
24     (or hypothesized) mental states or cognitive representations (e.g., Haxby et al., 2001; Huth et al., 2016, 2012;  
25     Kamitani & Tong, 2005; Mitchell et al., 2008; Nishimoto et al., 2011; Norman et al., 2006; Pereira et al.,  
26     2018; Tong & Pratte, 2012). Training decoding models on different types of neural features (Fig. 1a) can  
27     also help to elucidate which specific aspects of neural activity patterns are informative about cognition—  
28     and, by extension, which types of neural activity patterns might comprise the neural code. For example,  
29     prior work has used region of interest analyses to estimate the anatomical locations of specific neural  
30     representations (e.g., Etzel et al., 2009), or to compare the relative contributions to the neural code of

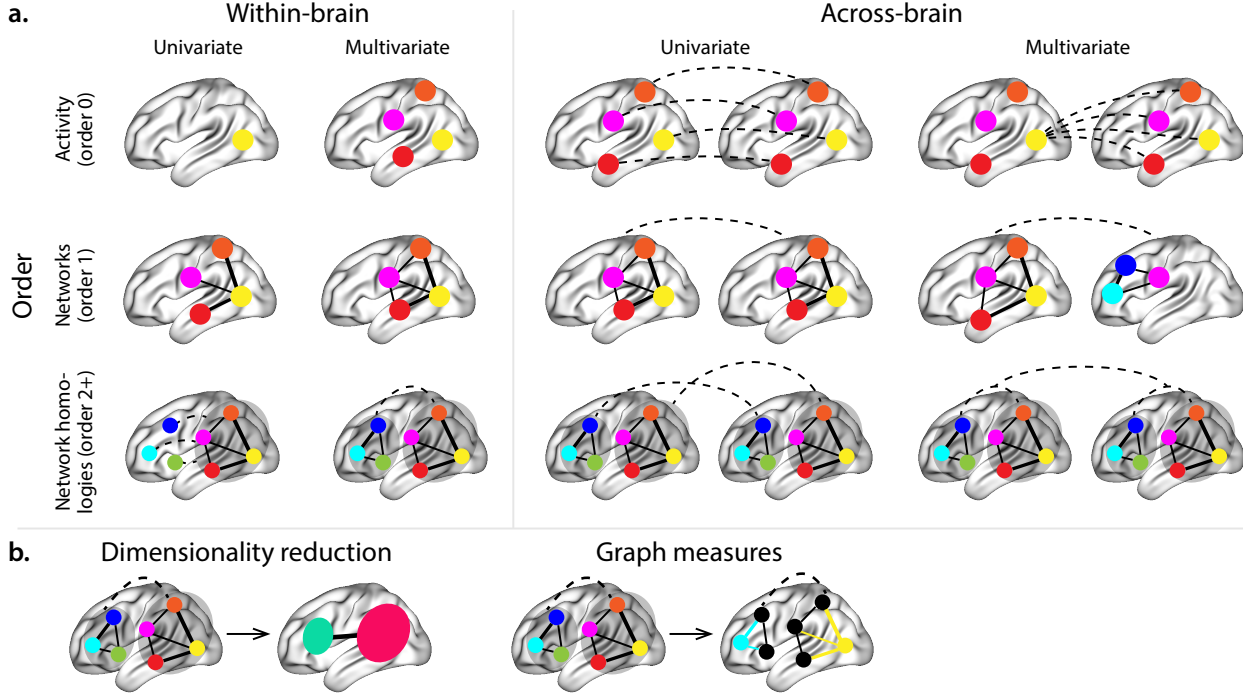


**Figure 1: Neural patterns. a. A space of neural analyses** Within-brain analyses are carried out within a single brain, whereas across-brain analyses compare neural patterns across two or more individuals' brains. Univariate analyses characterize the activities of individual units (e.g., nodes, small networks, hierarchies of networks, etc.), whereas multivariate analyses characterize the patterns of activities across units. Order 0 patterns involve individual nodes; order 1 patterns involve node-node interactions; order 2 (and higher) patterns relate to interactions between homologous networks. Each of these patterns may be static (e.g., averaging over time) or dynamic. **b. Summarizing neural patterns.** To efficiently compute with complex neural patterns, it can be useful to characterize the patterns using summary measures. Dimensionality reduction algorithms project the patterns onto lower-dimensional spaces whose dimensions reflect weighted combinations of the dimensions in the original space. Graph measures characterize each unit's participation in its associated network.

31 multivariate activity patterns versus patterns of dynamic correlations between neural activity patterns (e.g.,  
 32 Fong et al., 2019; Manning et al., 2018). An emerging theme in this literature is that cognition is mediated  
 33 by complex dynamic interactions between brain structures (Bassett et al., 2006; Demertzi et al., 2019; Sporns  
 34 & Honey, 2006; Turk-Browne, 2013).

35 Studies of the neural code to date have primarily focused on univariate or multivariate neural pat-  
 36 terns (for review see Norman et al., 2006), or (more recently) on patterns of dynamic first-order corre-  
 37 lations (i.e., interactions between pairs of brain structures; Fong et al., 2019; Manning et al., 2018). We  
 38 wondered what the future of this line of work might hold. For example, is the neural code mediated by  
 39 higher-order interactions between brain structures? Second-order correlations reflect *homologous* patterns of  
 40 correlation. In other words, if the changing patterns of correlations between two regions, *A* and *B*, are similar  
 41 to those between two other regions, *C* and *D*, this would be reflected in the second-order correlations be-

42 tween ( $A-B$ ) and ( $C-D$ ). In this way, second-order correlations identify similarities and differences between  
43 subgraphs of the brain’s connectome. Analogously, third-order correlations reflect homologies between  
44 second-order correlations— i.e., homologous patterns of homologous interactions between brain regions.  
45 More generally, higher-order correlations reflect homologies between patterns of lower-order correlations.  
46 We can then ask: which “orders” of interaction are most reflective of high-level cognitive processes?

47 Another central question pertains to the extent to which the neural code is carried by activity patterns  
48 that directly reflect ongoing cognition (e.g., following Haxby et al., 2001; Norman et al., 2006), versus the  
49 dynamic properties of the network structure itself, independent of specific activity patterns in any given  
50 set of regions (e.g., following Bassett et al., 2006). For example, graph measures such as centrality and  
51 degree (Bullmore & Sporns, 2009) may be used to estimate how a given brain structure is “communicating”  
52 with other structures, independently of the specific neural representations carried by those structures.  
53 If one considers a brain region’s position in the network (e.g., its eigenvector centrality) as a dynamic  
54 property, one can compare how the positions of different regions are correlated, and/or how those patterns  
55 of correlations change over time. We can also compute higher-order patterns in these correlations to  
56 characterize homologous subgraphs in the connectome that display similar changes in their constituent  
57 brain structures’ interactions with the rest of the brain.

58 To gain insights into the above aspects of the neural code, we developed a computational framework  
59 for estimating dynamic high-order correlations in timeseries data. This framework provides an important  
60 advance, in that it enables us to examine patterns in higher-order correlations that are computationally  
61 intractable to estimate via conventional methods. Given a multivariate timeseries, our framework provides  
62 timepoint-by-timepoint estimates of the first-order correlations, second-order correlations, and so on (up  
63 to tenth-order correlations in this manuscript). Our approach combines a kernel-based method for com-  
64 puting dynamic correlations in timeseries data with a dimensionality reduction step (Fig. 1b) that projects  
65 the resulting dynamic correlations into a low-dimensional space. We explored two dimensionality reduc-  
66 tion approaches: principle components analysis (PCA; Pearson, 1901), which preserves an approximately  
67 invertible transformation back to the original data; and a second non-invertible algorithm that explored  
68 patterns in eigenvector centrality (Landau, 1895). This latter approach characterizes correlations between  
69 each feature dimension’s relative *position* in the network in favor of the specific activity histories of different  
70 features.

71 We validated our approach using synthetic data where the underlying correlations were known. We  
72 then applied our framework to a neuroimaging dataset collected as participants listened to either an audio  
73 recording of a ten-minute story or a temporally scrambled version of the story, or underwent a resting state  
74 scan (Simony et al., 2016). We used a subset of the data to train across-participant classifiers to decode

75 listening times using a blend of neural features (comprising neural activity patterns, as well as different  
76 orders of correlations between those patterns that were inferred using our computational framework).  
77 We found that both the PCA-based and eigenvector centrality-based approaches yielded neural patterns  
78 that could be used to decode accurately. Both approaches also yielded the best decoding accuracy for  
79 data collected during (intact) story listening when high-order (PCA: second-order; eigenvector centrality:  
80 fourth-order) dynamic correlation patterns were included as features. When we trained classifiers on the  
81 scrambled stories or resting state data, only lower-order dynamic patterns were informative to the decoders.  
82 Taken together, our results indicate that high-level cognition is supported by high-order dynamic patterns  
83 of communication between brain structures.

## 84 Methods

85 Our general approach to comprises four general steps (Fig. 2). First, we derive a kernel-based approach  
86 to computing dynamic pairwise correlations in a  $T$  (timepoints) by  $K$  (features) multivariate timeseries,  
87  $\mathbf{X}_0$ . This yields a  $T$  by  $O(K^2)$  matrix of dynamic correlations,  $\mathbf{Y}_1$ , where each row comprises the upper  
88 triangle of the correlation matrix at a single timepoint, reshaped into a row vector (this reshaped vector is  
89  $(\frac{K^2-K}{2})$ -dimensional). Second, we apply a dimensionality reduction step to project the matrix of dynamic  
90 correlations back onto a  $K$ -dimensional space. This yields a  $T$  by  $K$  matrix,  $\mathbf{X}_1$ , that reflects an approximation  
91 of the dynamic correlations reflected in the original data. Third, we use repeated applications of the kernel-  
92 based dynamic correlation step to  $\mathbf{X}_n$  and the dimensionality reduction step to the resulting  $\mathbf{Y}_{n+1}$  to estimate  
93 high-order dynamnic correlations. Each application of these steps to a  $T$  by  $K$  time series  $\mathbf{X}_n$  yields a  $T$  by  $K$   
94 matrix,  $\mathbf{X}_{n+1}$ , that reflects the dynamic correlations between the columns of  $\mathbf{X}_n$ . In this way, we refer to  $n$  as  
95 the *order* of the timeseries, where  $\mathbf{X}_0$  (order 0) denotes the original data and  $\mathbf{X}_n$  denotes  $n^{\text{th}}$ -order dynamic  
96 correlations between the columns of  $\mathbf{X}_0$ . Finally, we use a cross-validation-based decoding approach to  
97 evaluate how well information contained in a given order (or weighted mixture of orders) may be used  
98 to decode relevant cognitive states. If including a given  $\mathbf{X}_n$  in the feature set yields higher classification  
99 accuracy on held-out data, we interpret this as evidence that the given cognitive states are reflected in  
100 patterns of  $n^{\text{th}}$ -order correlations. All of the code used to produce the figures and results in this manuscript,  
101 along with links to the corresponding datasets, may be found at [github.com/ContextLab/timecorr-paper](https://github.com/ContextLab/timecorr-paper). In  
102 addition, we have released a Python toolbox for computing dynamic high-order correlations in timeseries  
103 data; our toolbox may be found at [timecorr.readthedocs.io](https://timecorr.readthedocs.io). **JRM NOTE: CHECK LINK**

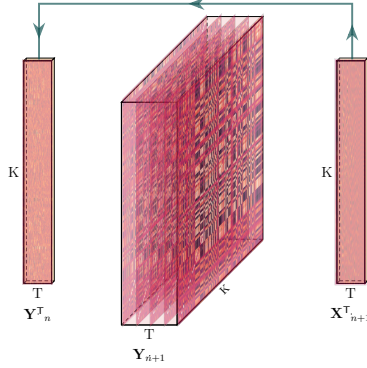


Figure 2: **Estimating dynamic high-order correlations.** Given a  $T$  by  $K$  matrix of multivariate timeseries data,  $\mathbf{Y}_n$  (where  $n \in \mathbb{N}, n \geq 0$ ), we use Equation 5 to compute a timeseries of  $K$  by  $K$  correlation matrices,  $\mathbf{Y}_{n+1}$ . We then approximate  $\mathbf{Y}_{n+1}$  with the  $T$  by  $K$  matrix  $\mathbf{X}_{n+1}$ . This process may be repeated to scalably estimate iteratively higher-order correlations in the data. Note that the transposes of  $\mathbf{Y}_n$  and  $\mathbf{X}_{n+1}$  are displayed in the figure for compactness.

104 **Kernel-based approach for computing dynamic correlations**

Given a matrix of observations, we can compute the (static) Pearson's correlation between any pair of columns,  $\mathbf{X}(\cdot, i)$  and  $\mathbf{X}(\cdot, j)$  using (Pearson, 1901):

$$\text{corr}(\mathbf{X}(\cdot, i), \mathbf{X}(\cdot, j)) = \frac{\sum_{t=1}^T (\mathbf{X}(t, i) - \bar{\mathbf{X}}(\cdot, i))(\mathbf{X}(t, j) - \bar{\mathbf{X}}(\cdot, j))}{\sqrt{\sum_{t=1}^T \sigma_{\mathbf{X}(\cdot, i)}^2 \sigma_{\mathbf{X}(\cdot, j)}^2}}, \text{ where} \quad (1)$$

$$\bar{\mathbf{X}}(\cdot, k) = \sum_{t=1}^T \mathbf{X}(t, k), \text{ and} \quad (2)$$

$$\sigma_{\mathbf{X}(\cdot, k)}^2 = \sum_{t=1}^T (\mathbf{X}(t, k) - \bar{\mathbf{X}}(\cdot, k))^2 \quad (3)$$

- 105 We can generalize this formula to compute time-varying correlations by incorporating a *kernel function* that  
 106 takes a time  $t$  as input, and returns how much the observed data at each timepoint  $\tau \in [-\infty, \infty]$  contributes  
 107 to the estimated instantaneous correlation at time  $t$  (Fig. 3).

Given a kernel function  $\kappa_t(\cdot)$  for timepoint  $t$ , evaluated at timepoints  $\tau \in [1, \dots, T]$ , we can update the

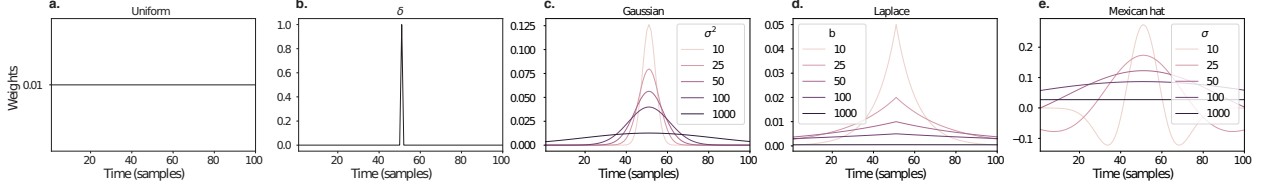


Figure 3: **Examples of kernel functions.** Each panel displays per-timepoint weights at  $t = 50$ , evaluated for 100 timepoints ( $\tau \in [1, \dots, 100]$ ). **a. Uniform kernel.** The weights are timepoint-invariant; observations at all timepoints are weighted equally, and do not change as a function of  $\tau$ . This is a special case of weight function that reduces dynamic correlations to static correlations. **b. Dirac  $\delta$  kernel.** Only the observation at timepoint  $t$  is given a non-zero weight (of 1). **c. Gaussian kernels.** Each kernel's weights fall off in time according to a Gaussian probability density function centered on time  $t$ . Weights derived using several different example width parameters ( $\sigma^2$ ) are displayed. **d. Laplace kernels.** Each kernel's weights fall off in time according to a Laplace probability density function centered on time  $t$ . Weights derived using several different example width parameters ( $b$ ) are displayed. **e. Mexican hat (Ricker wavelet) kernels.** Each kernel's weights fall off in time according to a Ricker wavelet centered on time  $t$ . This function highlights the *contrasts* between local versus surrounding activity patterns in estimating dynamic correlations. Weights derived using several different example width parameters ( $\sigma$ ) are displayed.

static correlation formula in Equation 2 to estimate the *instantaneous correlation* at timepoint  $t$ :

$$\text{timecorr}_{\kappa_t}(\mathbf{X}(\cdot, i), \mathbf{X}(\cdot, j)) = \frac{\sum_{\tau=1}^T (\mathbf{X}(\tau, i) - \tilde{\mathbf{X}}_{\kappa_t}(i))(\mathbf{X}(\tau, j) - \tilde{\mathbf{X}}_{\kappa_t}(j))}{\sqrt{\sum_{\tau=1}^T \tilde{\sigma}_{\kappa_t}^2(\mathbf{X}(\cdot, i))\tilde{\sigma}_{\kappa_t}^2(\mathbf{X}(\cdot, j))}}, \text{ where} \quad (4)$$

$$\tilde{\mathbf{X}}_{\kappa_t}(t, k) = \sum_{\tau=1}^T \kappa_t(\tau, k) \mathbf{X}(\tau, k), \quad (5)$$

$$\tilde{\sigma}_{\kappa_t}^2(\mathbf{X}(\cdot, k)) = \sum_{\tau=1}^T (\mathbf{X}(\tau, k) - \tilde{\mathbf{X}}_{\kappa_t}(t, k))^2. \quad (6)$$

108 Here  $\text{timecorr}(\mathbf{X}(\cdot, i), \mathbf{X}(\cdot, j), \kappa_t)$  reflects the correlation at time  $t$  between columns  $i$  and  $j$  of  $\mathbf{X}$ , estimated using  
 109 the kernel  $\kappa_t$ . We evaluate Equation 5 in turn each pair of columns in  $\mathbf{X}$  and for kernels centered on each  
 110 timepoint in the timeseries, respectively, to obtain a  $T$  by  $K$  by  $K$  timeseries of dynamic correlations,  $\mathbf{Y}$ . For  
 111 convenience, we then reshape the upper triangles of each timepoint's correlation matrix into a row vector  
 112 to obtain an equivalent  $T$  by  $\frac{K^2-K}{2}$  matrix.

### 113 Dynamic inter-subject functional connectivity (DISFC)

Equation 5 provides a means of taking a single observation matrix,  $\mathbf{X}_n$  and estimating the dynamic correlations from moment to moment,  $\mathbf{Y}_{n+1}$ . Suppose that one has access to a set of multiple observation matrices that reflect the same phenomenon. For example, one might collect neuroimaging data from several experimental participants, as each participant performs the same task (or sequence of tasks). Let  $\mathbf{X}_n^1, \mathbf{X}_n^2, \dots, \mathbf{X}_n^P$  reflect the  $T$  by  $K$  observation matrices ( $n = 0$ ) or reduced correlation matrices ( $n > 0$ ) for each of

$P$  participants in an experiment. We can use *inter-subject functional connectivity* (ISFC; Simony et al., 2016) to compute the degree of stimulus-driven correlations reflected in the multi-participant dataset at a given timepoint  $t$  using:

$$\bar{\mathbf{C}}(t) = M \left( R \left( \frac{1}{2P} \sum_{p=1}^P Z(Y_n^p(t))^T + Z(Y_n^p(t)) \right) \right), \quad (7)$$

where  $M$  extracts and vectorizes the diagonal and upper triangle of a symmetric matrix,  $Z$  is the Fisher z-transformation (Zar, 2010):

$$Z(r) = \frac{\log(1+r) - \log(1-r)}{2} \quad (8)$$

$R$  is the inverse of  $Z$ :

$$R(z) = \frac{\exp(2z-1)}{\exp(2z+1)}, \quad (9)$$

and  $\mathbf{Y}_n^p(t)$  denotes the correlation matrix (Eqn. 2) between each column of  $\mathbf{X}_n^p$  and each column of the average  $\mathbf{X}_n$  from all *other* participants,  $\bar{\mathbf{X}}_n^{ \setminus p}$ :

$$\bar{\mathbf{X}}_n^{ \setminus p} = R \left( \frac{1}{P-1} \sum_{q \in \setminus p} Z(\mathbf{x}_n^q) \right), \quad (10)$$

where  $\setminus p$  denotes the set of all participants other than participant  $p$ . In this way, the  $T$  by  $\frac{K^2-K}{2}$  DISFC matrix  $\bar{\mathbf{C}}$  provides a time-varying extension of the ISFC approach developed by Simony et al. (2016).

## 116 Low-dimensional representations of dynamic correlations

Given a  $T$  by  $\frac{K^2-K}{2}$  matrix of dynamic correlations,  $\mathbf{Y}_n$ , we propose two general approaches to computing a  $T$  by  $K$  low-dimensional representation of these correlations,  $\mathbf{X}_n$ . The first approach uses dimensionality reduction algorithms to project  $\mathbf{Y}_n$  onto a  $K$ -dimensional space. The second approach uses graph measures to characterize the relative positions of each feature ( $k \in [1, \dots, K]$ ) in the network defined by the correlation matrix at each timepoint.

### 122 Dimensionality reduction-based approaches to computing $\mathbf{X}_n$

The modern library of dimensionality reduction algorithms include Principal Components Analysis (PCA; Pearson, 1901), Probabilistic PCA (PPCA; Tipping & Bishop, 1999), Exploratory Factor Analysis (EFA;

125 Spearman, 1904), Independent Components Analysis (ICA; Comon et al., 1991; Jutten & Herault, 1991),  
126 *t*-Stochastic Neighbor Embedding (*t*-SNE; van der Maaten & Hinton, 2008), Uniform Manifold Approximation and Projection (UMAP; McInnes & Healy, 2018), non-negative matrix factorization (NMF; Lee &  
127 Seung, 1999), Topographic Factor Analysis (TFA) Manning et al. (2014), Hierarchical Topographic Factor  
128 analysis (HTFA) Manning et al. (2018), Topographic Latent Source Analysis (TLSA) Gershman et al. (2011),  
129 Dictionary learning (J. Mairal et al., 2009; J. B. Mairal et al., 2009), deep autoencoders (Hinton & Salakhutdinov, 2006), among others. While complete characterizations of each of these algorithms is beyond the scope  
130 of the present manuscript, the general intuition driving these approaches is to compute the  $T$  by  $I$  matrix,  
131  $\mathbf{X}$ , that is closest to the original  $T$  by  $J$  matrix,  $\mathbf{Y}$ , where (typically)  $I \ll J$ . The different approaches place  
132 different constraints on what properties  $\mathbf{X}$  must satisfy and which aspects of the data are compared (and  
133 how) to characterize the match between  $\mathbf{X}$  and  $\mathbf{Y}$ .

136 Applying dimensionality reduction algorithms to  $\mathbf{Y}$  yields a  $\mathbf{X}$  whose columns reflect weighted combinations  
137 (or nonlinear transformations) of the original columns of  $\mathbf{Y}$ . This has two main consequences. First,  
138 with each repeated dimensionality reduction, the resulting  $\mathbf{X}_n$  has lower and lower fidelity (with respect to  
139 what the “true”  $\mathbf{Y}_n$  might have looked like without using dimensionality reduction to maintain scalability).  
140 In other words, computing  $\mathbf{X}_n$  is a lossy operation. Second, whereas each columns of  $\mathbf{Y}_n$  may always be  
141 mapped directly onto specific pairs of columns of  $\mathbf{Y}_{n-1}$ , the columns of  $\mathbf{X}_n$  reflect weighted combinations  
142 and/or nonlinear transformations of the columns of  $\mathbf{Y}_n$ . Many dimensionality reduction algorithms are  
143 invertible (or approximately invertible). However, attempting to map a given  $\mathbf{X}_n$  back onto the original  
144 feature space of  $\mathbf{Y}_0$  will usually require  $O(TK^{2n})$  space and therefore quickly becomes intractable as  $n$  or  $K$   
145 grow large.

#### 146 **Graph measure approaches to computing $\mathbf{X}_n$**

147 The above dimensionality reduction approaches to approximating a given  $\mathbf{Y}_n$  with a lower-dimensional  
148  $\mathbf{X}_n$  preserve a (potentially recombined and transformed) mapping back to the original data in  $\mathbf{Y}_0$ . We  
149 also explore graph measure approaches that forgo a preserved mapping back to the original data in favor  
150 of preserving each feature’s relative *position* in the broader network of interactions and connections. To  
151 illustrate the distinction between the two general approaches we explore, suppose a network comprises  
152 nodes  $A$ ,  $B$ , and  $C$ . If  $A$  and  $B$  exhibit uncorrelated activity patterns, the functional connection between  
153 them will be (by definition) close to 0. However, if  $A$  and  $B$  each interact with  $C$  in similar ways, we might  
154 attempt to capture those similarities using a measure that reflects the how  $A$  and  $B$  interact in the network.

155 In general, graph measures take as input a matrix of interactions (e.g., using the above notation, an  $K$

156 by  $K$  correlation matrix or binarized correlation matrix reconstituted from a single timepoint's row of  $\mathbf{Y}$ )  
157 and return as output a set of  $K$  measures describing how each node (feature) sits within that correlation  
158 matrix with respect to the rest of the population. Widely used measures include betweenness centrality (the  
159 proportion of shortest paths between each pair of nodes in the population that involves the given node in  
160 question; e.g., Barthélemy, 2004; Freeman, 1977; Geisberger et al., 2008; Newman, 2005; Opsahl et al., 2010);  
161 diversity and dissimilarity (characterizations of how differently connected a given node is from others in  
162 the population; e.g., Lin, 2009; Rao, 1982; Ricotta & Szeidl, 2006); Eigenvector centrality and pagerank  
163 centrality (measures of how influential a given node is within the broader network; e.g., Bonacich, 2007;  
164 Halu et al., 2013; Lohmann et al., 2010; Newman, 2008); transfer entropy and flow coefficients (a measure  
165 of how much information is flowing from a given node to other nodes in the network; e.g., Honey et  
166 al., 2007; Schreiber, 2000);  $k$ -coreness centrality (a measure of the connectivity of a node within its local  
167 sub-graph; e.g., Alvarez-Hamelin et al., 2005; Christakis & Fowler, 2010); within-module degree (a measure  
168 of how many connections a node has to its close neighbors in the network; e.g., Rubinov & Sporns, 2010);  
169 participation coefficient (a measure of the diversity of a node's connections to different sub-graphs in the  
170 network; e.g., Rubinov & Sporns, 2010); and sub-graph centrality (a measure of a node's participation in  
171 all of the network's sub-graphs; e.g., Estrada & Rodríguez-Velázquez, 2005); among others.

172 For a given graph measure,  $\eta : \mathbb{R}^{K \times K} \rightarrow \mathbb{R}^K$ , we can use  $\eta$  to transform each row of  $\mathbf{Y}_n$  in a way that  
173 characterizes the corresponding graph properties of each column. This results in a new  $T$  by  $K$  matrix,  $\mathbf{X}_n$ ,  
174 that reflects how the features reflected in the columns of  $\mathbf{Y}_n$  participate in the network during each timepoint  
175 (row).

## 176 Dynamic higher-order correlations

177 Because  $\mathbf{X}_n$  has the same shape as the original data  $\mathbf{X}_0$ , approximating  $\mathbf{Y}_n$  with a lower-dimensional  $\mathbf{X}_n$   
178 enables us to estimate high-order dynamic correlations in a scalable way. Given a  $T$  by  $K$  input matrix, the  
179 output of Equation 5 requires  $O(TK^2)$  space to store. Repeated applications of Equation 5 (i.e., computing  
180 dynamic correlations between the columns of the outputted dynamic correlation matrix) each require  
181 exponentially more space; in general the  $n^{\text{th}}$ -order dynamic correlations of a  $T$  by  $K$  timeseries occupies  
182  $O(TK^{2n})$  space. However, when we approximate or summarize the output of Equation 5 with a  $T$  by  $K$  matrix  
183 (as described above), it becomes feasible to compute even very high-order correlations in high-dimensional  
184 data. Specifically, approximating the  $n^{\text{th}}$ -order dynamic correlations of a  $T$  by  $K$  timeseries requires only  
185  $O(TK^2)$  additional space— the same as would be required to compute first-order dynamic correlations. In  
186 other words, the space required to store  $n + 1$  multivariate timeseries reflecting up to  $n^{\text{th}}$  order correlations

187 in the original data scales linearly with  $n$  using our approach (Fig. 2).

## 188 Data

189 We examined two types of data: synthetic data and human functional neuroimaging data. We constructed  
190 and leveraged the synthetic data to evaluate our general approach. Specifically, we tested how well  
191 Equation 5 could be used to recover known dynamic correlations using different choices of kernel ( $\kappa$ ; Fig. 3),  
192 for each of several synthetic datasets that exhibited different temporal properties. We applied our approach  
193 to a functional neuroimaging dataset to test the hypothesis that ongoing cognitive processing is reflected  
194 in high-order dynamic correlations. We used an across-participant classification test to estimate whether  
195 dynamic correlations of different orders contain information about which timepoint in a story participants  
196 were listening to.

### 197 Synthetic data

198 We constructed a total of 40 multivariate timeseries, collectively reflecting a total of 4 different patterns of  
199 dynamic correlations (i.e., 10 datasets reflecting each type of dynamic pattern). Each timeseries comprised  
200 50 features (dimensions) that varied over 300 timepoints. The observations at each timepoint were drawn  
201 from a zero-mean multivariate Gaussian distribution with a covariance matrix defined for each timepoint  
202 as described below. We drew the observations at each timepoint independently from the draws at all other  
203 timepoints; in other words, for each observation  $s_t \sim \mathcal{N}(\mathbf{0}, \Sigma_t)$  at timepoint  $t$ ,  $p(s_t) = p(s_t | p_{\setminus t})$ .

**Constant.** We generated data with stable underlying correlations to evaluate how Equation 5 characterized correlation “dynamics” when the ground truth correlations were static. We constructed 10 multivariate timeseries, whose observations were each drawn from a single (stable) Gaussian distribution. For each dataset, we constructed a random covariance matrix,  $\Sigma_m$ :

$$\mathbf{C}(i, j) \sim \mathcal{N}(0, 1) \tag{11}$$

$$\Sigma_m = \mathbf{C}\mathbf{C}^\top, \text{ where} \tag{12}$$

204  $i, j \in [1, 2, \dots, 50]$ . In other words, all of the observations (for each of the 300 timepoints) within each dataset  
205 were drawn from a multivariate Gaussian distribution with the same covariance matrix, and the 10 datasets  
206 each used a different covariance matrix.

207 **Random.** We generated a second set of 10 synthetic datasets whose observations at each timepoint were  
208 drawn from a Gaussian distribution with a new randomly constructed (using Eqn. 12) covariance matrix.  
209 Because each timepoint’s covariance matrix was drawn independently of the covariance matrices for all  
210 other timepoints, these datasets provided a test of reconstruction accuracy in the absence of any meaningful  
211 underlying temporal structure in the dynamic correlations underlying the data.

**Ramping.** We generated a third set of 10 synthetic datasets whose underlying correlations changed gradually over time. For each dataset, we constructed two *anchor* correlation matrices using Equation 12,  $\Sigma_{\text{start}}$  and  $\Sigma_{\text{end}}$ . For each of the 300 timepoints in each dataset, we drew the observations from a multivariate Gaussian distribution whose covariance matrix at each timepoint  $t \in [0, \dots, 299]$  was given by

$$\Sigma_t = \left(1 - \frac{1-t}{299}\right)\Sigma_{\text{start}} + \frac{t}{299}\Sigma_{\text{end}}. \quad (13)$$

212 The gradually changing correlations underlying these datasets allow us to evaluate the recovery of dynamic  
213 correlations when each timepoint’s correlation matrix is unique (as in the random datasets), but where the  
214 correlation dynamics are structured.

215 **Event.** We generated a fourth set of 10 synthetic datasets whose underlying correlation matrices exhibited  
216 prolonged intervals of stability, interspersed with abrupt changes. For each dataset, we used Equation ??  
217 to generate 5 random covariance matrices. We constructed a timeseries where each set of 60 consecutive  
218 samples was drawn from a Gaussian with the same covariance matrix. These datasets were intended to  
219 simulate a system that undergoes occasional abrupt state changes.

## 220 Functional neuroimaging data collected during story listening

221 We examined an fMRI dataset collected by Simony et al. (2016) that the authors have made publically  
222 available at [arks.princeton.edu/ark:/88435/dsp015d86p269k](http://arks.princeton.edu/ark:/88435/dsp015d86p269k). The dataset comprises neuroimaging data  
223 collected as participants listened to an audio recording of a story (intact condition; 36 participants), listened  
224 to time scrambled recordings of the same story (17 participants in the paragraph-scrambled condition  
225 listened to the paragraphs in a randomized order and 36 in the word-scrambled condition listened to  
226 the words in a randomized order), or lay resting with their eyes open in the scanner (rest condition; 36  
227 participants). Full neuroimaging details may be found in the original paper for which the data were  
228 collected (Simony et al., 2016).

229 **Hierarchical topographic factor analysis (HTFA).** Following our prior related work, we used HTFA (Manning et al., 2018) to derive a compact representation of the data. In brief, this approach approximates the  
230 timeseries of voxel activations (44,415 voxels) using a much smaller number of radial basis function (RBF)  
231 nodes (in this case 700 nodes). This provides a convenient representation for examining full-brain network  
232 dynamics. All of the analyses we carried out on the neuroimaging dataset were performed in this lower-  
233 dimensional space. In other words, each participant’s data matrix,  $Y_0$ , was a number-of-timepoints by 700  
234 matrix of HTFA-derived factor weights (where the row and column labels were matched across partici-  
235 pants). Code for carrying out HTFA on fMRI data may be found as part of the BrainIAK toolbox (Capota et  
236 al., 2017), which may be downloaded at [brainiak.org](http://brainiak.org).  
237

## 238 **Temporal decoding**

239 We sought to identify neural patterns that reflected participants’ ongoing cognitive processing of incoming  
240 stimulus information. As reviewed by Simony et al. (2016), one way of homing in on these stimulus-driven  
241 neural patterns is to compare activity patterns across individuals (e.g., using ISFC analyses). In particular,  
242 neural patterns will be similar across individuals, to the extent that the neural patterns under consideration  
243 are stimulus driven, and to the extent that the corresponding cognitive representations are reflected in similar  
244 spatial patterns across people. Following this logic, we used an across-participants temporal decoding test  
245 developed by Manning et al. (2018) to assess the degree to which different neural patterns reflected ongoing  
246 stimulus-driven cognitive processing across people. The approach entails using a subset of the data to  
247 train a classifier to decode which stimulus timepoint (i.e., moment in the story participants listened to). We  
248 use decoding (forward inference) accuracy on held-out data, from held-out participants, as a proxy for the  
249 extent to which the inputted neural patterns reflected stimulus-driven cognitive processing in a similar way  
250 across individuals.

### 251 **Forward inference and decoding accuracy**

252 We used an across-participants correlation-based classifier to decode which stimulus timepoint matched a  
253 given neural pattern. We first divided the participants into two groups: a template group,  $\mathcal{G}_{\text{template}}$ , and a  
254 to-be-decoded group,  $\mathcal{G}_{\text{decode}}$ . We used Equation 7 to compute a DISFC matrix for each group ( $\bar{\mathbf{C}}_{\text{template}}$  and  
255  $\bar{\mathbf{C}}_{\text{decode}}$ , respectively). We then correlated the rows of  $\bar{\mathbf{C}}_{\text{template}}$  and  $\bar{\mathbf{C}}_{\text{decode}}$  to form a number-of-timepoints by  
256 number-of-timepoints decoding matrix,  $\Lambda$ . In this way, the rows of  $\Lambda$  reflected timepoints from the template  
257 group, while the columns reflected timepoints from the to-be-decoded group. We assigned temporal labels  
258 to each row  $\bar{\mathbf{C}}_{\text{decode}}$  using the row of  $\bar{\mathbf{C}}_{\text{template}}$  to which it was most highly correlated. We then repeated

259 this decoding procedure, but using  $\mathcal{G}_{\text{decode}}$  as the template group and  $\mathcal{G}_{\text{template}}$  as the to-be-decoded group.  
260 Given the true timepoint labels (for each group), we defined the *decoding accuracy* as the proportion of  
261 correctly decoded timepoints, across both groups.

262 **Feature weighting and testing**

263 We sought to examine which types of neural features (i.e., activations, first-order dynamic correlations, and  
264 higher-order dynamic correlations) were informative to the temporal decoders. Using the notation above,  
265 these features correspond to  $\mathbf{Y}_0, \mathbf{X}_1, \mathbf{X}_2, \mathbf{X}_3$ , and so on (we examined up to tenth order correlations, or  $\mathbf{X}_{10}$ ).

266 One challenge to fairly evaluating high-order correlations is that if the kernel used in Equation 5 is  
267 wider than a single timepoint, each repeated application of the equation will result in further temporal  
268 blur. Because our primary assessment metric is temporal decoding accuracy, this unfairly biases against  
269 detecting meaningful signal in higher-order correlations (relative to lower-order correlations). We attempted  
270 to mitigate temporal blur in estimating each  $\mathbf{X}_n$  by using a Dirac  $\delta$  function kernel (which places all of its  
271 mass over a single timepoint; Fig. 3b) to compute each lower-order correlation ( $\mathbf{X}_1, \mathbf{X}_2, \dots, \mathbf{X}_{n-1}$ ). We then used  
272 a (potentially wider, as described below) kernel to compute  $\mathbf{X}_n$  from  $\mathbf{X}_{n-1}$ . In this way, temporal blurring  
273 was applied only in the last step of computing  $\mathbf{X}_n$ . We note that, because each  $\mathbf{X}_n$  is a low-dimensional  
274 representation of the corresponding  $\mathbf{Y}_n$ , the higher-order correlations we estimated reflect true correlations  
275 in the data with lower-fidelity than estimates of lower-order correlations.

276 After computing each  $\mathbf{X}_1, \mathbf{X}_2, \dots, \mathbf{X}_{n-1}$  for each participant, we divided participants into two equally sized  
277 groups ( $\pm 1$  for odd numbers of participants):  $\mathcal{G}_{\text{train}}$  and  $\mathcal{G}_{\text{test}}$ . We then further subdivided  $\mathcal{G}_{\text{train}}$  into  $\mathcal{G}_{\text{train}_1}$   
278 and  $\mathcal{G}_{\text{train}_2}$ . We then computed  $\Lambda$  temporal correlation matrices for each type of neural feature, using  $\mathcal{G}_{\text{train}_1}$   
279 and  $\mathcal{G}_{\text{train}_2}$ . This resulted in  $n + 1$   $\Lambda$  matrices (one for the original timeseries of neural activations, and one  
280 for each of  $n$  orders of dynamic correlations). Our objective was to find a set of weights of each of these  $\Lambda$   
281 matrices such that the weighted average of the  $n + 1$  matrices yielded the highest decoding accuracy. We  
282 used quasi-Newton gradient ascent (Nocedal & Wright, 2006), using decoding accuracy as the objective  
283 function to be maximized, to find an optimal set of training data-derived weights,  $\phi_{0,1,\dots,n}$ , where  $\sum_{i=0}^n \phi_i = 1$   
284 and where  $\phi_i \geq 0 \forall i \in [0, 1, \dots, n]$ .

285 After estimating an optimal set of weights, we computed a new set of  $n + 1$   $\Lambda$  matrices correlating the  
286 DISFC patterns from  $\mathcal{G}_{\text{train}}$  and  $\mathcal{G}_{\text{test}}$  at each timepoint. We use the resulting decoding accuracy of  $\mathcal{G}_{\text{test}}$   
287 timepoints to estimate how informative the set up neural features containing up to  $n^{\text{th}}$  order correlations  
288 were.

289 We used a permutation-based procedure to form a stable estimate of decoding accuracy for each set of

290 neural features. In particular, we computed the decoding accuracy for each of 10 random group assignments  
291 of  $\mathcal{G}_{\text{train}}$  and  $\mathcal{G}_{\text{test}}$ . We report the mean accuracy (and 95% confidence intervals) for each set of neural features.

292 **Identifying robust decoding results**

293 The temporal decoding procedure we use to estimate which neural features support ongoing cognitive  
294 processing is governed by many parameters. For example, Equation 5 requires defining a kernel function,  
295 which can take on different shapes and widths. For a fixed set of neural features, each of these parameters  
296 can yield different decoding accuracies. Further, the best decoding accuracy for a given timepoint may be  
297 reliably achieved by one set of parameters, whereas the best decoding accuracy for another timepoint might  
298 be reliably achieved by a different set of parameters, and the best decoding accuracy across *all* timepoints  
299 might be reliably achieved by still another different set of parameters. Rather than attempting to maximize  
300 decoding accuracy, we sought to discover the trends in the data that were robust to specific classifier  
301 parameters choices. Specifically, we sought to characterize how decoding accuracy varied (under different  
302 experimental conditions) as a function of which neural features were considered.

303 To identify decoding results that were robust to specific classifier parameter choices, we repeated our  
304 decoding analyses that substituted in a variety of kernel shapes and widths for Equation 5. We examined  
305 Gaussian (Fig. 3c), Laplace (Fig. 3d), and Mexican Hat (Fig. 3e) kernels, each with widths of 5, 10, 20, and  
306 50 samples. We then report the average decoding accuracies across all of these parameter choices. This  
307 enabled us to (roughly) factor out performance characteristics that were parameter dependent (within the  
308 space of parameters we examined).

309 **Reverse inference**

310 The dynamic patterns we examine comprise high-dimensional correlation patterns at each timepoint. To  
311 help interpret the resulting patterns in the context of other studies, we created summary maps by computing  
312 the across-timepoint average pairwise correlations at each order of analysis (first order, second order, etc.,  
313 up to fifteenth order correlations). We selected the 10 strongest (absolute value) correlations at each order.  
314 Each correlation is between the dynamic activity patterns (or patterns of dynamic high-order correlations)  
315 measured at two RBF nodes (see *Hierarchical Topographic Factor Analysis*). Therefore, the 10 strongest  
316 correlations involved up to 20 RBF nodes. Each RBF defines a spatial function whose activations range  
317 from 0 to 1. We thresholded each RBF at 0.999 to construct a map of spherical components that denoted the  
318 endpoints of the 10 strongest correlations. We then carried out a meta analysis using Neurosynth (Rubin et  
319 al., 2017) to identify the 10 terms most commonly associated with the given map. This resulted in a set of

320 10 terms associated with the average dynamic correlation patterns at each order.

## 321 Results

322 We sought to understand whether high-level cognition is supported by dynamic patterns of high-order  
323 correlations. To that end, we developed a computational framework for estimating the dynamics of high-  
324 order correlations in multivariate timeseries data (see *Dynamic inter-subject functional connectivity (DISFC)*  
325 and *Dynamic higher-order correlations*). We evaluated the efficacy of this framework at recovering known  
326 patterns in several synthetic datasets (see *Synthetic data*). We then applied the framework to a public fMRI  
327 dataset collected as participants listened to an auditorily presented story, a temporally scrambled version  
328 of the story, or underwent a resting state scan (see *Functional neuroimaging data collected during story listening*).  
329 We used the relative decoding accuracies of classifiers trained on different sets of neural features to estimate  
330 which types of features reflected ongoing cognitive processing.

### 331 Recovering known dynamic correlations from synthetic data

332 We generated synthetic datasets that differed in how the underlying correlations changed over time. For  
333 each dataset, we applied Equation 5 with a variety of kernel shapes and widths. We assessed how well  
334 the true underlying correlations at each timepoint matched the recovered correlations (Fig. 4). For every  
335 kernel and dataset we tested, our approach recovered the correlation dynamics we embedded into the data.  
336 However, the quality of these recoveries varied across different synthetic datasets in a kernel-dependent  
337 way.

338 In general, wide monotonic kernels (Laplace, Gaussian) performed best when the correlations varied  
339 gradually from moment-to-moment (Figs. 4a, c, and d). **TODO: Say something about kernel widths within**  
340 **a shape.** In the extreme, as the rate of change in correlations approaches 0 (Fig. 4a), an infinitely wide kernel  
341 would exactly recover the Pearson's correlation (e.g., compare Eqns. 2 and 5).

342 When the correlation dynamics were unstructured in time (Fig. 4b), a Dirac  $\delta$  kernel (infinitely narrow)  
343 performed best. This is because, when every timepoint's correlations are independent of the correlations in  
344 every other timepoint, averaging data over time dilutes the available signal. **TODO: Say something about**  
345 **kernel widths within a shape.**

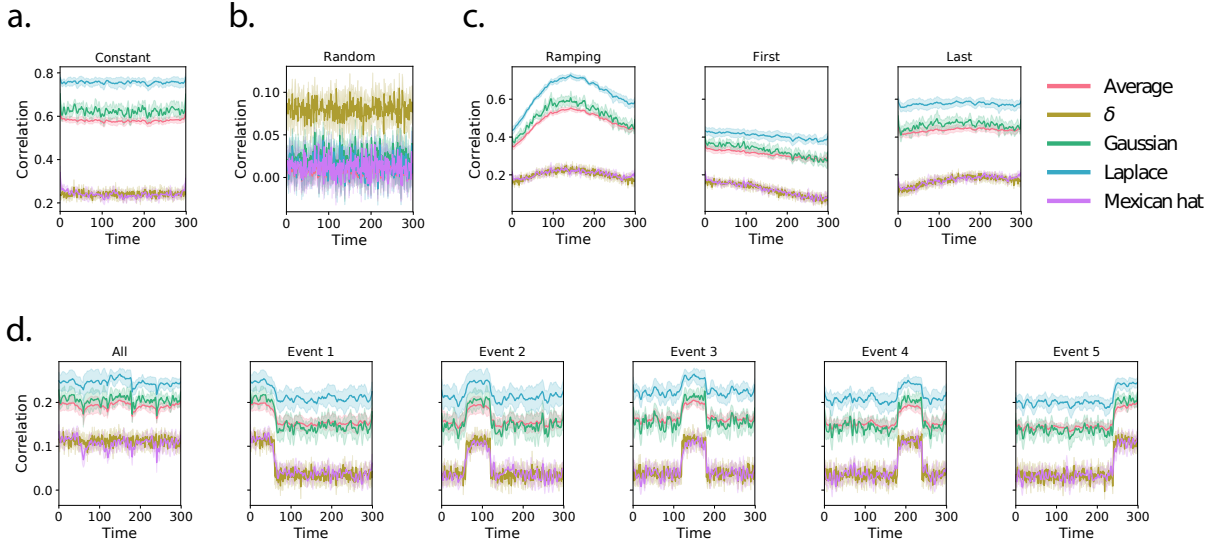


**Figure 4: Recovering known dynamic correlations from synthetic data.** Each panel displays the average correlations between the vectorized upper triangles of the recovered correlation matrix at each timepoint and either the true underlying correlation at each timepoint or a reference correlation matrix. (The averages are taken across 10 different randomly generated synthetic datasets of the given category.) Error ribbons denote 95% confidence intervals (taken across datasets). Different colors denote different kernel shapes, whereas the shading within each color type denotes kernel widths. For a complete description of each synthetic dataset, see *Synthetic data*. **a. Constant correlations.** These datasets have a stable (unchanging) underlying correlation matrix. **b. Random correlations.** These datasets are generated using a new independently drawn correlation matrix at each new timepoint. **c. Ramping correlations.** These datasets are generated by smoothly varying the underlying correlations between the randomly drawn correlation matrices at first and last timepoints. The left panel displays the correlations between the recovered dynamic correlations and the underlying ground truth correlations. The middle panel compares the recovered correlations with the *first* timepoint’s correlation matrix. The right panel compares the recovered correlations with the *last* timepoint’s correlation matrix. **d. Event-based correlations.** These datasets are each generated using five randomly drawn correlation matrices that each remain stable for a fifth of the total timecourse. The left panel displays the correlations between the recovered dynamic correlations and the underlying ground truth correlations. The right panels compare the recovered correlations with the correlation matrices unique to each event.

346 **Cognitively relevant dynamic high-order correlations in fMRI data**

347 We used across-participant temporal decoders to identify cognitively relevant neural patterns in fMRI data  
348 (see *Forward inference and decoding accuracy*). The dataset we examined (collected by Simony et al., 2016)  
349 comprised four experimental conditions that exposed participants to stimuli that varied systematically in  
350 how cognitively engaging they were. The *intact* experimental condition had participants listen to an audio  
351 recording of a 10-minute story. The *paragraph*-scrambled experimental condition had participants listen to a  
352 temporally scrambled version of the story, where the paragraphs occurred out of order (but where the same  
353 total set of paragraphs were presented over the full listening interval). All participants in this condition  
354 experienced the scrambled paragraphs in the same order. The *word*-scrambled experimental condition had  
355 participants listen to a temporally scrambled version of the story where the words in the story occurred in a  
356 random order. All participants in the word conditions experienced the scrambled words in the same order.  
357 Finally, in a *rest* experimental condition participants lay in the scanner with no overt stimulus, with their  
358 eyes open (blinking as needed). This dataset provided a convenient means of testing our hypothesis that  
359 different levels of cognitive engagement might be supported by different orders of complex brain activity  
360 dynamics.

361 In brief, we computed timeseries of dynamic high-order correlations that were similar across participants  
362 in each of two randomly assigned groups: a training group and a test group. We then trained classifiers  
363 on the training group's data to match each sample from the test group with a stimulus timepoint. Each  
364 classifier comprised a weighted blend of neural patterns that reflected up to  $n^{\text{th}}$ -order dynamic correlations  
365 (see *Feature weighting and testing*). We repeated this process for  $n \in \{0, 1, 2, \dots, 10\}$ . Our examinations of  
366 synthetic data suggested that none of the kernels we examined were "universal" in the sense of optimally  
367 recovering underlying correlations regardless of the structure of those correlations. In our analyses of neural  
368 data, we therefore averaged our decoding results over a variety of kernel shapes and widths in order to  
369 identify results that were robust to specific kernel parameters (also see *Identifying robust decoding results*).

370 Our approach to estimating dynamic high-order correlations requires mapping the high-dimensional  
371 feature space of correlations (a  $T$  by  $O(K^2)$  matrix) onto a lower-dimensional  $T$  by  $K$  matrix. We carried out  
372 two sets of analyses that differed in how this mapping was computed. The first set of analyses used PCA  
373 to find a low-dimensional embedding of the original dynamic correlation matrices (Fig. 5a,b). The second  
374 set of analyses characterized correlations in dynamics of each feature's eigenvector centrality, but did not  
375 preserve the underlying activity dynamics (Fig. 5c,d).

376 Both sets of temporal decoding analyses yielded qualitatively similar results for the auditory (non-  
377 rest) conditions of the experiment (Fig. 5: pink, yellow, and teal lines). The highest decoding accuracy

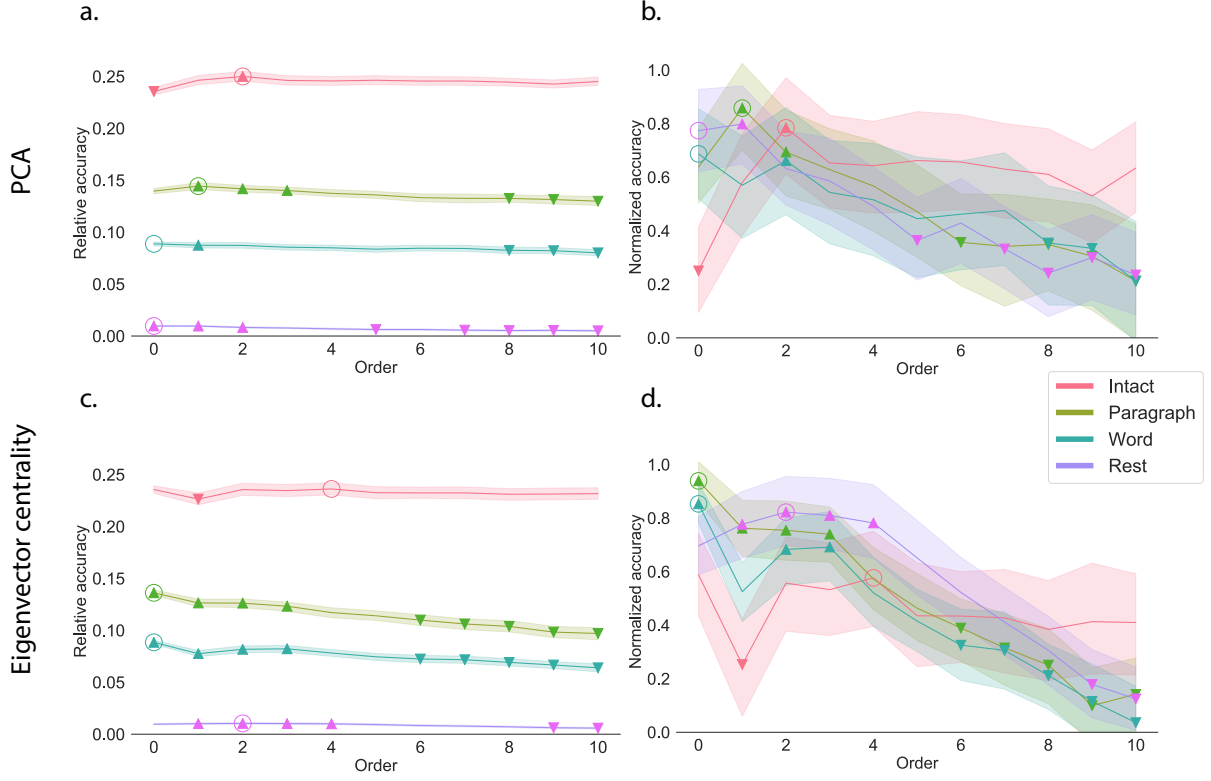


**Figure 5: Across-participant decoding accuracy varies with correlation order and cognitive engagement.**

**a. Decoding accuracy as a function of order: PCA.** Order (x-axis) refers to the maximum order of dynamic correlations that were available to the classifiers (see *Feature weighting and testing*). The reported across-participant decoding accuracies are averaged over all kernel shapes and widths (see *Identifying robust decoding results*). The y-values are displayed relative to chance accuracy (intact:  $\frac{1}{300}$ ; paragraph:  $\frac{1}{272}$ ; word:  $\frac{1}{300}$ ; rest:  $\frac{1}{400}$ ). The error bars denote 95% confidence intervals across cross-validation folds (i.e., random assignments of participants to the training and test sets). The colors denote the experimental condition. Arrows denote sets of features that yielded reliably higher (upwards facing) or lower (downward facing) decoding accuracy than the mean of all other features (via a two-tailed test, thresholded at  $p < 0.05$ ). The circled values represent the maximum decoding accuracy within each experimental condition.

**b. Normalized decoding accuracy as a function of order: PCA.** This panel displays the same results as Panel a, but here each curve has been normalized to have a maximum value of 1 and a minimum value of 0 (including the upper and lower bounds of the respective 95% confidence intervals). Panels a and b used PCA to project each high-dimensional pattern of dynamic correlations onto a lower-dimensional space.

**c. Decoding accuracy as a function of order: eigenvector centrality.** This panel is in the same format as Panel a, but here eigenvector centrality has been used to project the high-dimensional patterns of dynamic correlations onto a lower-dimensional space.

**d. Normalized decoding accuracy as a function of order: eigenvector centrality.** This panel is in the same format as Panel b, but here eigenvector centrality has been used to project the high-dimensional patterns of dynamic correlations onto a lower-dimensional space.

378 for participants who listened to the intact (unscrambled) story was achieved using high-order dynamic  
379 correlations (PCA: second-order; eigenvector-centrality: fourth-order). Scrambled versions of the story were  
380 best decoded by lower-order correlations (PCA/paragraph: first-order; PCA/word: order zero; eigenvector  
381 centrality/paragraph: order zero; eigenvector centrality/word: order zero). The two sets of analyses yielded  
382 different decoding results on resting state data (Fig. 5: purple lines). We note could be decoded only very  
383 slightly above chance; we speculate that the decoders might have picked up on attentional drift, boredom,  
384 or tiredness; we hypothesize these all increase throughout the resting state scan. Our decoders might  
385 be picking up on aspects of these loosely defined cognitive states that are common across individuals. The  
386 PCA-based approach achieved the highest resting state decoding accuracy using order zero features (non-  
387 correlational activation-based), whereas the eigenvector centrality-based approach achieved the highest  
388 resting state decoding accuracy using second-order correlations. Taken together, these analyses indicate  
389 that high-level cognitive processing (while listening to the intact story) is reflected in the dynamics of high-  
390 order correlations in brain activity, whereas lower-level cognitive processing (while listening to scrambled  
391 versions of the story that lack rich meaning) is reflected in the dynamics of lower-order correlations and  
392 non-correlational activity dynamics. Further, these patterns are associated both with the underlying activity  
393 patterns (characterized using PCA) and also with the changing relative positions that different brain areas  
394 occupy in their associated networks (characterized using eigenvector centrality).

395 Having established that patterns of high-order correlations are informative to decoders, we next won-  
396 dered which specific networks of brain regions contributed most to these patterns. As a representative  
397 example, we selected the kernel parameters that yielded decoding accuracies that best matched the average  
398 accuracies across all of the kernel parameters we examined. Using Figure ??c as a template, the best-  
399 matching kernel was a Laplace kernel with a width of 50 (Fig. 3d). We used this kernel to compute a single  
400  $K$  by  $K$   $n^{\text{th}}$ -order correlation matrix for each experimental condition, along with the Neurosynth (Rubin et  
401 al., 2017) terms most highly associated with each of these matrices (Fig. 6; see *Reverse inference*).

402 For all of the story listening conditions (intact, paragraph, and word), we found that first- and second-  
403 order correlations were most strongly associated with auditory and speech processing. During intact story  
404 listening, third-order correlations reflected integration with visual areas, and fourth-order correlations  
405 reflected integration with areas associated with high-level cognition and cognitive control, such as the ven-  
406 tralateral prefrontal cortex. However, during listening to temporally scrambled stories, these higher-order  
407 correlations instead involved interactions with additional regions associated with speech and semantic pro-  
408 cessing. By contrast, we found a much different set of patterns in the resting state data. First-order resting  
409 state correlations were most strongly associated with regions involved in counting and numerical under-  
410 standing. Second-order resting state correlations were strongest in visual areas; third-order correlations

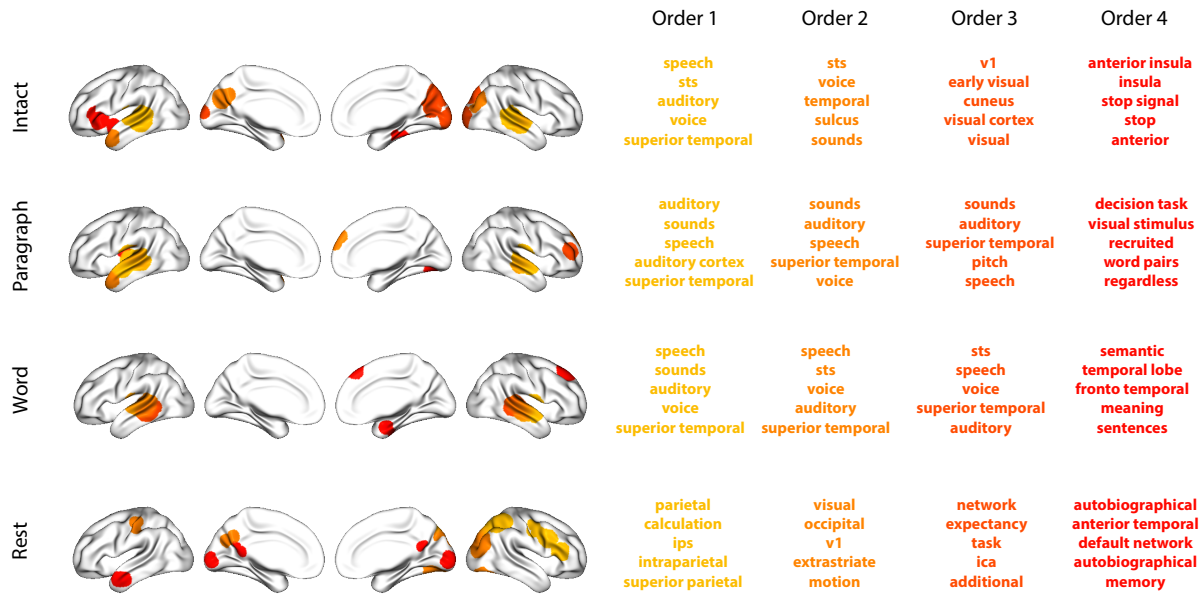


**Figure 6: Top terms associated with the endpoints of the strongest correlations.** Each color corresponds to one order of correlations, averaged across participants and time. The inflated brain plots display the locations of the endpoints of the 10 strongest (absolute value) correlations at each order, projected onto the cortical surface (Combrisson et al., 2019). The lists of terms on the right display the top five Neurosynth terms (Rubin et al., 2017) decoded from the corresponding brain maps for each order. Each row displays data from a different experimental condition. Additional maps and their corresponding Neurosynth terms may be found in the *Supplementary materials* (intact: Figure S1; paragraph: Figure S2; word: Figure S3; rest: Figure S4).

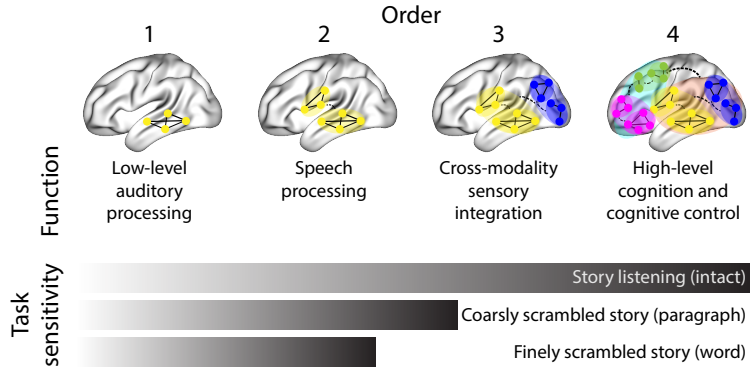


**Figure 7: Proposed high-order network dynamics underlying high-level cognition.** Higher orders of network interactions support higher-level aspects of cognitive processing. When tasks evoke richer, deeper, and/or higher-level processing, this is reflected in higher-order network interactions.

were strongest in task-positive areas; and fourth-order correlations were strongest in regions associated with autobiographical and episodic memory. We carried out analogous analyses to create maps (and decode the top associated Neurosynth terms) for up to fifteenth-order correlations (Figs. S1, S2, S3, and S4). Of note, examining fifteenth-order correlations between 700 nodes using conventional methods would have required storing roughly  $\frac{700^{2 \times 15}}{2} \approx 1.13 \times 10^{85}$  floating point numbers—assuming single-precision (32 bits each), this would require roughly 32 times as many bits as there are molecules in the known universe! Although these fifteenth-order correlations do appear (visually) to have some well-formed structure, we provide this latter example primarily as a demonstration of the efficiency and scalability of our approach.

## 419 Discussion

We tested the hypothesis that high-level cognition is supported by high-order brain network dynamics. We examined high-order network dynamics in functional neuroimaging data collected during a story listening experiment. When participants listened to an auditory recording of the story, participants exhibited similar high-order brain network dynamics. By contrast, when participants instead listened to temporally scrambled recordings of the story, only lower-order brain network dynamics were similar across participants. Our results indicate that higher orders of network interactions support higher-level aspects of cognitive processing (Fig.7).

Identifying higher-order network dynamics associated with high-level cognition required several important methods advances. First, we used kernel-based dynamic correlations to extend the notion of (static) inter-subject functional connectivity (Simony et al., 2016) to a dynamic measure of inter-subject functional connectivity (DISFC) that does not rely on sliding windows, and that may be computed at individual

431 timepoints. This allowed us to precisely characterize stimulus-evoked network dynamics that were similar  
432 across individuals. Second, we developed a computational framework for efficiently and scalably estimat-  
433 ing high-order dynamic correlations. Our approach uses dimensionality reduction algorithms and graph  
434 measures to obtain low-dimensional embeddings of patterns of network dynamics. Third, we developed  
435 an analysis framework for identifying robust decoding results by carrying out our analyses using a range  
436 of parameter values and then identifying which results were robust to specific parameter choices.

437 Relevant literature:

- 438 • ?: more complex concepts involve more complex network dynamics
- 439 • Demertzi et al. (2019): human consciousness is supported by dynamic complex patterns of brain  
440 signal coordination. studied the brains of healthy vs minimally conscious patients; conscious patients  
441 displayed richer and more structured patterns of network interactions
- 442 • Mack et al. (2017): richer task structure is supported by more complex (higher rank) brain patterns in  
443 the prefrontal cortex
- 444 • ?: review of time-varying connectivity
- 445 • ?: higher variability in dynamic functional connectivity predicts worse attention. also, dynamic  
446 functional connectivity improves attention predictions over static functional connectivity.
- 447 • ?: dynamic causal modelling: compute causal interaction dynamics in multivariate timeseries data.  
448 important to consider causation in interpreting the direction of information flow reflected in the  
449 patterns we identified through our analyses.
- 450 • ?: another review of time varying connectivity
- 451 • Roy et al. (2019): memories are distributed across functionally connected brain areas
- 452 • Fallon et al. (2019): the timescale of spontaneous resting state fMRI increases with structural connec-  
453 tivity strength (in mouse and human brains)
- 454 • Liégeois et al. (2019): dynamic resting state functional connectivity best captures task-based phe-  
455 notypes (processing speed, fluid intelligence), whereas static and dynamic functional connectivity  
456 equally capture self-reported measures like loneliness and life satisfaction. suggest that different  
457 timescales of connectivity dynamics reflect different aspects of behavior.
- 458 • Zheng et al. (2019): characterize brain connectomes at different geometric scales

- 459 • McIntosh & Jirsa (2019): neural processes reflect system interactions that occur on relatively low-  
460 dimensional manifolds, thereby constraining possible functional configurations. (motivation for di-  
461 mensionality reduction approach?)
- 462 • Toker & Sommer (2019): another approach to reducing dimensionality of network interactions, using  
463 spectral clustering
- 464 • Zou et al. (2019): another review of complex network dynamics in timeseries data
- 465 • Shappell et al. (2019): state-based analyses of network dynamics using hidden semi-Markov models.  
466 could be a useful direction for extended our work; for example, we could define kernel functions to  
467 only integrate within an “event.” This could potentially improve resolution of event-specific network  
468 dynamics.
- 469 • Cole et al. (2019): potential artifacts or spurious insights that affect standard functional connectivity  
470 analyses (not sure this applies)
- 471 • ?: simulations for benchmarking time-varying connectivity methods (should we use this? seems  
472 useful! could potentially replace synthetic data section)
- 473 • Chang & Glover (2010)
- 474 • Sizemore et al. (2018)
- 475 • Reimann et al. (2017)
- 476 • Gonzalez-Castillo et al. (2019)
- 477 • Betzel et al. (2019)

## 478 Acknowledgements

479 We acknowledge discussions with Luke Chang, Hany Farid, Paxton Fitzpatrick, Andrew Heusser, Eshin  
480 Jolly, Qiang Liu, Matthijs van der Meer, Judith Mildner, Gina Notaro, Stephen Satterthwaite, Emily Whitaker,  
481 Weizhen Xie, and Kirsten Ziman. Our work was supported in part by NSF EPSCoR Award Number 1632738  
482 to J.R.M. and by a sub-award of DARPA RAM Cooperative Agreement N66001-14-2-4-032 to J.R.M. The  
483 content is solely the responsibility of the authors and does not necessarily represent the official views of our  
484 supporting organizations.

485 **Author contributions**

486 Concept: J.R.M. Implementation: T.H.C., L.L.W.O., and J.R.M. Analyses: L.L.W.O and J.R.M.

487 **References**

- 488 Alvarez-Hamelin, I., Dall'Asta, L., Barrat, A., & Vespignani, A. (2005). *k*-corr decomposition: a tool for the  
489 visualiztion of large scale networks. *arXiv*, cs/0504107v2.
- 490 Barthélemy, M. (2004). Betweenness centrality in large complex networks. *European Physical Journal B*, 38,  
491 163–168.
- 492 Bassett, D., Meyer-Lindenberg, A., Achard, S., Duke, T., & Bullmore, E. (2006, December). Adaptive  
493 reconfiguration of fractal small-world human brain functional networks. *Proceedings of the National  
494 Academy of Sciences, USA*, 103(51), 19518–23.
- 495 Betzel, R. F., Byrge, L., Esfahlani, F. Z., & Kennedy, D. P. (2019). Temporal fluctuations in the brain's modular  
496 architecture during movie-watching. *bioRxiv*, doi.org/10.1101/750919.
- 497 Bonacich, P. (2007). Some unique properties of eigenvector centrality. *Social Networks*, 29(4), 555–564.
- 498 Bullmore, E., & Sporns, O. (2009). Complex brain networks: graph theoretical analysis of structural and  
499 functional systems. *Nature Reviews Neuroscience*, 10(3), 186–198.
- 500 Capota, M., Turek, J., Chen, P.-H., Zhu, X., Manning, J. R., Sundaram, N., . . . Shin, Y. S. (2017). *Brain imaging  
501 analysis kit*. Retrieved from <https://doi.org/10.5281/zenodo.59780>
- 502 Chang, C., & Glover, G. H. (2010). Time-frequency dynamics of resting-state brain connectivity measured  
503 with fMRI. *NeuroImage*, 50, 81–98.
- 504 Christakis, N. A., & Fowler, J. H. (2010). Social network sensors for early detection of contagious outbreaks.  
505 *PLoS One*, 5(9), e12948.
- 506 Cole, M. W., Ito, T., Schultz, D., Mill, R., Chen, R., & Cocuzza, C. (2019). Task activations produce spurious  
507 but systematic inflation of task functional connectivity estimates. *NeuroImage*, 189, 1–18.
- 508 Combrisson, E., Vallat, R., O'Reilly, C., Jas, M., Pasarella, A., Saive, A., . . . Jerbi, K. (2019). Visbrain: a  
509 multi-purpose GPU-accelerated open-source suite for multimodal brain data visualization. *Frontiers in  
510 Neuroinformatics*, 13(14), 1–14.

- 511 Comon, P., Jutten, C., & Herault, J. (1991). Blind separation of sources, part II: Problems statement. *Signal*  
512 *Processing*, 24(1), 11 - 20.
- 513 Demertzi, A., Tagliazucchi, E., Dehaene, S., Deco, G., Barttfeld, P., Raimondo, F., ... Sitt, J. D. (2019). Human  
514 consciousness is supported by dynamic complex patterns of brain signal coordination. *Science Advances*,  
515 5(2), eaat7603.
- 516 Estrada, E., & Rodríguez-Velázquez, J. A. (2005). Subgraph centrality in complex networks. *Physical Review*  
517 *E*, 71(5), 056103.
- 518 Etzel, J. A., Gazzola, V., & Keysers, C. (2009). An introduction to anatomical ROI-based fMRI classification.  
519 *Brain Research*, 1282, 114–125.
- 520 Fallon, J., Ward, P., Parkes, L., Oldham, S., Arnatkevičiūtė, A., Fornito, A., & Fulcher, B. D. (2019).  
521 Timescales of spontaneous activity fluctuations relate to structural connectivity in the brain. *bioRxiv*,  
522 doi.org/10.1101/655050.
- 523 Fong, A. H. C., Yoo, K., Rosenberg, M. D., Zhang, S., Li, C.-S. R., Scheinost, D., ... Chun, M. M. (2019).  
524 Dynamic functional connectivity during task performance and rest predicts individual differences in  
525 attention across studies. *NeuroImage*, 188, 14–25.
- 526 Freeman, L. C. (1977). A set of measures of centrality based on betweenness. *Sociometry*, 40(1), 35–41.
- 527 Geisberger, R., Sanders, P., & Schultes, D. (2008). Better approximation of betweenness centrality. *Proceedings*  
528 *of the meeting on Algorithm Engineering and Experiments*, 90–100.
- 529 Gershman, S., Blei, D., Pereira, F., & Norman, K. (2011). A topographic latent source model for fMRI data.  
530 *NeuroImage*, 57, 89–100.
- 531 Gonzalez-Castillo, J., Caballero-Gaudes, C., Topolski, N., Handwerker, D. A., Pereira, F., & Bandettini, P. A.  
532 (2019). Imaging the spontaneous flow of thought: distinct periods of cognition contribute to dynamic  
533 functional connectivity during rest. *NeuroImage*, 202(116129).
- 534 Halu, A., Mondragón, R. J., Panzarasa, P., & Bianconi, G. (2013). Multiplex PageRank. *PLoS One*, 8(10),  
535 e78293.
- 536 Haxby, J. V., Gobbini, M. I., Furey, M. L., Ishai, A., Schouten, J. L., & Pietrini, P. (2001). Distributed and  
537 overlapping representations of faces and objects in ventral temporal cortex. *Science*, 293, 2425–2430.
- 538 Hinton, G. E., & Salakhutdinov, R. R. (2006). Reducing the dimensionality of data with neural networks.  
539 *Science*, 313(5786), 504–507.

- 540 Honey, C. J., Kötter, R., Breakspear, M., & Sporns, O. (2007). Network structure of cerebral cortex shapes  
541 functional connectivity on multiple time scales. *Proceedings of the National Academy of Science USA*, 104(24),  
542 10240–10245.
- 543 Huth, A. G., de Heer, W. A., Griffiths, T. L., Theunissen, F. E., & Gallant, J. L. (2016). Natural speech reveals  
544 the semantic maps that tile human cerebral cortex. *Nature*, 532, 453–458.
- 545 Huth, A. G., Nisimoto, S., Vu, A. T., & Gallant, J. L. (2012). A continuous semantic space describes  
546 the representation of thousands of object and action categories across the human brain. *Neuron*, 76(6),  
547 1210–1224.
- 548 Jutten, C., & Herault, J. (1991). Blind separation of sources, part I: An adaptive algorithm based on  
549 neuromimetic architecture. *Signal Processing*, 24(1), 1–10.
- 550 Kamitani, Y., & Tong, F. (2005). Decoding the visual and subjective contents of the human brain. *Nature*  
551 *Neuroscience*, 8, 679–685.
- 552 Landau, E. (1895). Zur relativen Wertbemessung der Turnierresultate. *Deutsches Wochenschach*, 11, 366–369.
- 553 Lee, D. D., & Seung, H. S. (1999). Learning the parts of objects by non-negative matrix factorization. *Nature*,  
554 401, 788–791.
- 555 Liégeois, R., Li, J., Kong, R., Orban, C., De Ville, D. V., Ge, T., … Yeo, B. T. T. (2019). Resting brain  
556 dynamics at different timescales capture distinct aspects of human behavior. *Nature Communications*,  
557 10(2317), doi.org/10.1038/s41467-019-10317-7.
- 558 Lin, J. (2009). Divergence measures based on the Shannon entropy. *IEEE Transactions on Information Theory*,  
559 37(1), 145–151.
- 560 Lohmann, G., Margulies, D. S., Horstmann, A., Pleger, B., Lepsien, J., Goldhahn, D., … Turner, R. (2010).  
561 Eigenvector centrality mapping for analyzing connectivity patterns in fMRI data of the human brain.  
562 *PLoS One*, 5(4), e10232.
- 563 Mack, M. L., Preston, A. R., & Love, B. C. (2017). Medial prefrontal cortex compresses concept representations  
564 through learning. *bioRxiv*, doi.org/10.1101/178145.
- 565 Mairal, J., Ponce, J., Sapiro, G., Zisserman, A., & Bach, F. R. (2009). Supervised dictionary learning. *Advances*  
566 *in Neural Information Processing Systems*, 1033–1040.
- 567 Mairal, J. B., Bach, F., Ponce, J., & Sapiro, G. (2009). Online dictionary learning for sparse coding. *Proceedings*  
568 *of the 26th annual international conference on machine learning*, 689–696.

- 569 Manning, J. R., Ranganath, R., Norman, K. A., & Blei, D. M. (2014). Topographic factor analysis: a Bayesian  
570 model for inferring brain networks from neural data. *PLoS One*, 9(5), e94914.
- 571 Manning, J. R., Zhu, X., Willke, T. L., Ranganath, R., Stachenfeld, K., Hasson, U., ... Norman, K. A. (2018).  
572 A probabilistic approach to discovering dynamic full-brain functional connectivity patterns. *NeuroImage*,  
573 180, 243–252.
- 574 McInnes, L., & Healy, J. (2018). UMAP: Uniform manifold approximation and projection for dimension  
575 reduction. *arXiv*, 1802(03426).
- McIntosh, A. R., & Jirsa, V. K. (2019). The hidden repertoire of brain dynamics and dysfunction. *Network  
Neuroscience*, doi.org/10.1162/netn\_a00107.
- 576 Mitchell, T., Shinkareva, S., Carlson, A., Chang, K., Malave, V., Mason, R., & Just, M. (2008). Predicting  
577 human brain activity associated with the meanings of nouns. *Science*, 320(5880), 1191.
- 578 Newman, M. E. J. (2005). A measure of betweenness centrality based on random walks. *Social Networks*, 27,  
579 39–54.
- 580 Newman, M. E. J. (2008). The mathematics of networks. *The New Palgrave Encyclopedia of Economics*, 2, 1–12.
- 581 Nishimoto, S., Vu, A., Naselaris, T., Benjamini, Y., Yu, B., & Gallant, J. (2011). Reconstructing visual  
582 experience from brain activity evoked by natural movies. *Current Biology*, 21, 1 - 6.
- 583 Nocedal, J., & Wright, S. J. (2006). *Numerical optimization*. New York: Springer.
- 584 Norman, K. A., Newman, E., Detre, G., & Polyn, S. M. (2006). How inhibitory oscillations can train neural  
585 networks and punish competitors. *Neural Computation*, 18, 1577–1610.
- 586 Opsahl, T., Agneessens, F., & Skvoretz, J. (2010). Node centrality in weighted networks: generalizing degree  
587 and shortest paths. *Social Networks*, 32, 245–251.
- 588 Pearson, K. (1901). On lines and planes of closest fit to systems of points in space. *The London, Edinburgh,  
589 and Dublin Philosophical Magazine and Journal of Science*, 2, 559-572.
- 590 Pereira, F., Lou, B., Pritchett, B., Ritter, S., Gershman, S. J., Kanwisher, N., ... Fedorenko, E. (2018). Toward  
591 a universal decoder of linguistic meaning from brain activation. *Nature Communications*, 9(963), 1–13.
- 592 Rao, C. R. (1982). Diversity and dissimilarity coefficients: a unified approach. *Theoretical Population Biology*,  
593 21(1), 24–43.

- 594 Reimann, M. W., Nolte, M., Scolamiero, M., Turner, K., Perin, R., Chindemi, G., ... Markram, H. (2017).  
595 Cliques of neurons bound into cavities provide a missing link between structure and function. *Frontiers*  
596 in *Computational Neuroscience*, 11(48), 1–16.
- 597 Ricotta, C., & Szeidl, L. (2006). Towards a unifying approach to diversity measures: Bridging the gap  
598 between the Shannon entropy and Rao's quadratic index. *Theoretical Population Biology*, 70(3), 237–243.
- 599 Roy, D. S., Park, Y.-G., Ogawa, S. K., Cho, J. H., Choi, H., Kamensky, L., ... Tonegawa, S. (2019). Brain-  
600 wide mapping of contextual fear memory engram ensembles supports the dispersed engram complex  
601 hypothesis. *bioRxiv*, doi.org/10.1101/668483.
- 602 Rubin, T. N., Kyoejo, O., Gorgolewski, K. J., Jones, M. N., Poldrack, R. A., & Yarkoni, T. (2017). Decoding  
603 brain activity using a large-scale probabilistic functional-anatomical atlas of human cognition. *PLoS*  
604 *Computational Biology*, 13(10), e1005649.
- 605 Rubinov, M., & Sporns, O. (2010). Complex network measures of brain connectivity: uses and interpreta-  
606 tions. *NeuroImage*, 52, 1059–1069.
- 607 Schreiber, T. (2000). Measuring information transfer. *Physical Review Letters*, 85(2), 461–464.
- 608 Shappell, H., Caffo, B. S., Pekar, J. J., & Lindquist, M. A. (2019). Improved state change estimation in  
609 dynamic functional connectivity using hidden semi-Markov models. *NeuroImage*, 191, 243–257.
- 610 Simony, E., Honey, C. J., Chen, J., & Hasson, U. (2016). Uncovering stimulus-locked network dynamics  
611 during narrative comprehension. *Nature Communications*, 7(12141), 1–13.
- 612 Sizemore, A. E., Giusti, C., Kahn, A., Vettel, J. M., Betzel, R. F., & Bassett, D. S. (2018). Cliques and cavities  
613 in the human connectome. *Journal of Computational Neuroscience*, 44(1), 115–145.
- 614 Spearman, C. (1904). General intelligence, objectively determined and measured. *American Journal of*  
615 *Psychology*, 15, 201–292.
- 616 Sporns, O., & Honey, C. J. (2006). Small worlds inside big brains. *Proceedings of the National Academy of*  
617 *Science USA*, 103(51), 19219–19220.
- 618 Tipping, M. E., & Bishop, C. M. (1999). Probabilistic principal component analysis. *Journal of Royal Statistical*  
619 *Society, Series B*, 61(3), 611–622.
- 620 Toker, D., & Sommer, F. T. (2019). Information integration in large brain networks. *PLoS Computational*  
621 *Biology*, 15(2), e1006807.

- 622 Tong, F., & Pratte, M. S. (2012). Decoding patterns of human brain activity. *Annual Review of Psychology*, 63,  
623 483–509.
- 624 Turk-Browne, N. B. (2013). Functional interactions as big data in the human brain. *Science*, 342, 580–584.
- 625 van der Maaten, L. J. P., & Hinton, G. E. (2008). Visualizing high-dimensional data using t-SNE. *Journal of  
626 Machine Learning Research*, 9, 2579–2605.
- 627 Zar, J. H. (2010). *Biostatistical analysis*. Prentice-Hall/Pearson.
- 628 Zheng, M., Allard, A., Hagmann, P., & Serrano, M. A. (2019). Geometric renormalization unravels self-  
629 similarity of the multiscale human connectome. *arXiv*, 1904.11793.
- 630 Zou, Y., Donner, R. V., Marwan, N., Donges, J. F., & Kurths, J. (2019). Complex network approaches to  
631 nonlinear time series analysis. *Physics Reports*, 787, 1–97.